

# Orbit Determination of PHA 2002 QF15

W. Beard, J. Hong, and G. Xin (Team #9)

July 25, 2019

## Abstract

The asteroid 2002 QF15 is observed from Mt. Etscorn observatory (MPC 719) with a 14" Celestron telescope. With four dates of observation, 2002 QF15's angular position and apparent magnitude are determined by means of Least Squares Plate Reduction (LSPR) and linear regression respectively. With the angular position of 2002 QF15 at various dates, the asteroid's six classical orbital elements are calculated, and the error in each is explored. The team's average orbital elements were all within 0.1% error of those of JPL. Finally, data from three of the observations was submitted to the Minor Planet Center on July 18, 2019.

# Contents

<b>1</b>	<b>Introduction</b>	<b>3</b>
<b>2</b>	<b>Materials and Methods</b>	<b>3</b>
2.1	Instruments and Software . . . . .	3
2.2	Observations . . . . .	3
2.3	Method of Calculation . . . . .	4
2.4	Method of Gauss . . . . .	4
2.5	Specifics of Orbit Determination . . . . .	5
<b>3</b>	<b>Data and Analysis</b>	<b>5</b>
3.1	Observational Data . . . . .	6
3.2	Astrometry . . . . .	6
3.3	Photometry . . . . .	7
3.4	Orbital Elements . . . . .	8
3.5	Description of Orbital Elements . . . . .	8
3.6	Comparison With Other Observational Data . . . . .	10
3.7	Differential Correction . . . . .	10
3.8	Monte Carlo Error . . . . .	11
3.9	Monte Carlo Adjustment . . . . .	12
3.10	Other Asteroid Characteristics . . . . .	13
3.11	Comparison With Known Values . . . . .	14
3.12	Near-Earth Asteroid Group . . . . .	14
<b>4</b>	<b>Conclusion</b>	<b>14</b>
<b>5</b>	<b>Appendices</b>	<b>14</b>
5.1	Minor Planet Center Report . . . . .	14
5.2	Cloudy Night Experiments . . . . .	15
5.2.1	Data Collection Strategy . . . . .	15
5.2.2	Methodology . . . . .	15
5.2.3	Hypotheses and Expected Results . . . . .	16
5.2.4	Cloudy Night One: Dependence of Dark Currents on Exposure Time. . . . .	16
5.2.5	Cloudy Night Two: Temperature Dependence of Dark Frames . . . . .	17
5.2.6	Cloudy Night Three: Constancy of the Bias Levels . . . . .	21
<b>6</b>	<b>Acknowledgements</b>	<b>22</b>

# 1 Introduction

2002 QF15 is a Near-Earth-Asteroid (NEA), an asteroid whose orbit comes closer to Earth than that of any planet. It is also a potentially hazardous asteroid (PHA), meaning that it is large enough in size to cause serious damage upon impact and comes dangerously close to Earth during its orbit. When asteroids of 2002 QF15's size collide with Earth, significant physical damage and biospheric consequences ensue. Such asteroids (2km in diameter) are speculated to have the same amount of kinetic energy as one million megatons of TNT and will very likely cause regional earthquakes, hurricanes, and even tsunamis. Because of the high level of risk surrounding PHAs, it is vital to track their orbits as accurately as possible so that future collisions can be predicted and even prevented.

To that end, we (SSP NMT '19 - Team #9 - Nuclear Pasta) observed 2002 QF15 from Mt. Etschorn Observatory at regular intervals and calculated both the angular position and apparent magnitude of 2002 QF15. While the apparent magnitude may seem unimportant in this context, brightness often corresponds to the size of an asteroid, an important factor in its impact damage. The output of LSPR is then used as input in an implementation of the Method of Gauss to determine a preliminary orbit of the asteroid. Afterwards, we examined the error in the preliminary orbit and attempted to reduce it. In addition, the observational data from three nights was sent to the Minor Planet Center so that it may be available to the rest of the scientific community and be used to better monitor 2002 QF15 in the future.

## 2 Materials and Methods

### 2.1 Instruments and Software

Teams, including us, at the Summer Science Program in Astrophysics (New Mexico Institute of Mining and Technology campus) observed at Etschorn Observatory for the duration of the program and used the observatory's Celestron C-14 telescope (aperture of 355.5mm and focal length of 3911mm) with a SBIG STL-11000M CCD Chip ( $4008 \times 2745$  array,  $9\mu\text{m}$  pixels, a gain of  $0.8e^-/\text{ADU}$  and a read noise of  $11e^-/\text{pix RMS}$ ) for observations. We used TheSkyX program at Etschorn Observatory to control the camera, telescope, and focuser, and to take images.

Prior to observing, each team member used the JPL Horizons Web-Interface to generate an ephemeris that predicts the right ascension, declination, altitude, azimuth, visual magnitude, and target-observer-moon angle in a 3-hour window centered on a 2-hour observing session. We used DS9 along with the Bright Star Catalogue, 5th Revised Ed. (Hoffleit+, 1991) to find focus stars within a radius of 5.0 degrees of the field center and with a visual magnitude between 3 and 6. Finally, we also used DS9 (SAO Image Servers) to obtain star charts for observing sessions to check our position within the sky.

After observing sessions, we used AstroImageJ to reduce, align, and blink our science images to identify our asteroids. AstroImageJ let us find our asteroid by "blinking" images, making motion apparent to an observer.

The DS9 software was also used in finding reference stars for our astrometry and photometry. We used the AAVSO Photometric All Sky Survey (APASS) DR9 catalogue (Henden+, 2016) for our photometry and the GAIA-II catalogue for our astrometry.

### 2.2 Observations

We went to Etschorn Observatory six times during June and July of 2019. Five out of the six trips resulted in a successful identification of 2002 QF15. Timing and weather conditions during three of the trips allowed for completion of all three cloudy night experiments (see Appendix B). We had clear skies for our first of three nights and partially cloudy skies for our final three nights. We exposed at 90 seconds for our first night, and then we switched to 120 seconds for the rest of the program. Similarly, we exposed in the visual filter for our first three observations and switched to clear filter during our third observation for more bright images. The telescope had 3x3 binning with no calibration setting and a focus generally between 2000 and 3000.

## 2.3 Method of Calculation

For observations during the summer of 2019, we opted to follow SSP’s recommendation of using the Method of Gauss to determine a preliminary orbit of 2002 QF15. The method of Gauss uses angular position and Earth-Sun vectors from three observations to determine a Sun-Asteroid Cartesian position and velocity vector. With more observations, the preliminary orbit can be improved to more accurately model the asteroid as it orbits the sun. The use of the word “preliminary” to describe orbits determined from the Method of Gauss distinguishes them from precise orbits, often those determined from more precise instrumentation and alternative methods of distance determination.

## 2.4 Method of Gauss

The Method of Gauss requires the following for each of three observations: time (in Julian Date), the right ascension of the object, the declination of the object, and an Earth-Sun vector. Ecliptic unit vectors are determined using

$$\begin{bmatrix} x \\ y \\ z \end{bmatrix} = \begin{bmatrix} 1 & 0 & 0 \\ 0 & \cos(\epsilon) & \sin(\epsilon) \\ 0 & -\sin(\epsilon) & \cos(\epsilon) \end{bmatrix} \cdot \begin{bmatrix} \cos(\alpha)\cos(\delta) \\ \cos(\alpha)\sin(\delta) \\ \sin(\delta) \end{bmatrix} \quad (1)$$

where  $\alpha$  is right ascension,  $\delta$  is declination, and  $\epsilon$  is the obliquity of Earth. Now, using the *Scalar Equation of Lagrange*, the magnitude of the Sun-Asteroid position vector can be estimated. For each reasonable root of

$$x^8 + ax^6 + bx^4 + c = 0 \quad (2)$$

where  $x$  is an estimated magnitude of the Sun-Asteroid position vector at the central observation, an iterative method can be employed to refine the Sun-Asteroid position vector and determine the Sun-Asteroid velocity vector. The fundamental idea behind the Method of Gauss is to translate observational unit vectors and Earth-Sun position vectors into a position and velocity of some object (2002 QF15 in this case). Using the *Fundamental Triangle* we can determine the desired Sun-Asteroid vectors from the Earth-Sun position vector.

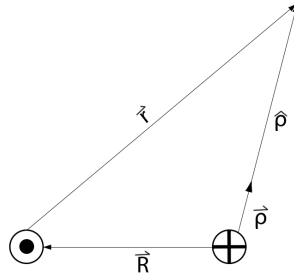


Figure 1: The Fundamental Triangle

The team opted to use results from *truncated Taylor polynomials* to refine the Sun-Asteroid vectors during the iteration process. The  $f$  and  $g$  series

$$f_i \approx 1 - \frac{\mu}{2r_2^3}\tau_i^2 + \frac{\mu(\vec{r}_2 \cdot \dot{\vec{r}}_2)}{2r_2^5}\tau_i^3 \quad (3)$$

$$g_i \approx \tau_i - \frac{\mu}{6r_2^3}\tau_i^3 \quad (4)$$

(where  $r_2$  is the magnitude of the Sun-Asteroid vector and  $\tau_i$  is the Gaussian time  $\tau$  at observation) can be used to determine constants and ultimately find the Sun-Asteroid vectors. While the first iteration can only use the first two terms of the  $f_i$  series, subsequent iterations can use the third term and even an expanded fourth term of the series. From  $f_1$ ,  $f_3$ ,  $g_1$ , and  $g_3$  (subscripts refer to the observation number), an updated Sun-Asteroid position vector can be determined from

$$\vec{r}_2 = \vec{\rho}_2 - \vec{R}_2 \quad (5)$$

where  $\rho_2$  relies on the  $f_i$  and  $g_i$  terms and  $\vec{R}_2$  is the Earth-Sun vector. From the same line of reasoning,  $\vec{r}_1$  and  $\vec{r}_3$  can be determined. Both allow

$$\dot{\vec{r}}_2 = d_1\vec{r}_1 + d_3\vec{r}_3 \quad (6)$$

to be used since  $d_1$  and  $d_3$  are other known constants from the  $f_i$  and  $g_i$  terms. Finally, each iteration requires a correction for the light travel time between the observing instrument and the object being observed. Because it takes the light reflected by 2002 QF15 some non-negligible amount of time to reach the observing instrument, 2002 QF15 has moved a non-negligible distance in space since that the light left it. To correct for this, the magnitude of the Earth-Asteroid position vector is used in correspondence with the speed of light to determine an actual time of observation. To put it simply,

$$t_i = t_{o,i} - \frac{\vec{\rho}_i}{c} \quad (7)$$

must be completed during each iteration (including the preliminary iteration) in the Method of Gauss to more accurately place the time of observation. As the Method of Gauss runs, the Sun-Asteroid vectors can either converge or diverge. In the case where the vectors diverge during iteration, different methods for determining the  $f_i$  and  $g_i$  terms must be employed. If, however, the Sun-Asteroid vectors converge (we defined convergence of the Sun-Asteroid vectors as a change of less than  $10^{-9}$  in between iterations), they can be used to determine the orbital elements of observed object using various formulae derived from Orbital Mechanics.

## 2.5 Specifics of Orbit Determination

Each of our team members selected three data points from different nights and ran his/her Method of Gauss code on the data. W. Beard opted to use 3rd degree Taylor polynomials while J. Hong and G. Xin chose 4th degree Taylor polynomials for their Orbit Determination code. Both methods seemed to yield relatively accurate orbital elements.

## 3 Data and Analysis

From our five asteroid observations, the following table was created to represent our astrometrically determined angular position and photometrically determined visual magnitude.

JD	RA	Declination	Vmag	Filter
2458654.66	14:28:02.03 $\pm$ 0.48	+23:21:44.8 $\pm$ 0.45	16.2	V
2458654.71	14:28:08.23 $\pm$ 0.41	+23:21:27.8 $\pm$ 0.34	16.4	V
2458660.66	14:40:13.76 $\pm$ 0.53	+22:44:54.0 $\pm$ 0.40	16.7	V
2458664.66	14:48:45.81 $\pm$ 0.27	+22:10:04.4 $\pm$ 0.28	17.1	C
2458664.70	14:48:50.85 $\pm$ 0.42	+22:09:39.9 $\pm$ 0.35	16.9	V
2458668.75	14:56:44.59 $\pm$ 0.19	+21:30:43.3 $\pm$ 0.26	17.1	C
2458668.78	14:56:47.62 $\pm$ 0.25	+21:30:25.8 $\pm$ 0.61	17.2	C
2458676.70	15:10:59.0 $\pm$ 0.65	+20:06:40.4 $\pm$ 0.81	17.5	C

Table 1: Observational RA, Dec, and Vmag

### 3.1 Observational Data

Using the C-14 telescope, we generated raw fits images at every observation session. In each session, we took light, dark, and bias images.

Light frames come in either clear or visual filters (as shown in Table 1, we used both), and contain the actual image data of the object being photographed, in our case, the PHA 2002 QF15. There are, however, a number of imperfections such as the thermal noise, vignetting, dust, bias signal, hot pixels etc. that need to be removed.

This leads us to take the dark and bias frames in addition to the light frames. Dark frames are images we took when covering the aperture of the telescope so no light could get in and we would have a picture with only hot pixels, thermal signal, random noise, and other non-random signals that we call dark signal. By subtracting the dark frames from the light frames we are “zeroing” them. It is important that the dark frames are taken at the same thermal temperature as the light frames since the thermal signal depends on temperature.

We take bias frames to remove the readout signal from the camera sensor since there is a variation in how the camera reads data from the sensor. The bias frames would be subtracted from all of lights, darks, and flats (and dark flats) before the stacking process to remove these variations. Bias frames are taken with lens cap on the telescope at zero exposure length and taken with the same ISO.

Finally, we have the flat frames. We did not take the flat frames ourselves; rather, the flats were provided by Dr Rangstorf et al. The flats are for correcting optical imperfections because most telescopes do not evenly distribute light across the camera sensor (causing the image to be brighter in the centre and darker near the edges, and also causing dark blotches to appear on the images). Flats can correct for this by taking pictures that are blank and evenly illuminated. Dividing the lights by the stacked flats evens out the illumination throughout the light frame.

### 3.2 Astrometry

With processed images, a procedure called Least Squares Plate Reduction (LSPR) can be employed to find a precise angular location of 2002 QF15 and an uncertainty in that position. LSPR works

by performing simultaneous  $\chi^2$  minimization on the fit of  $x, y$  locations to  $\alpha, \delta$  values. The input to LSPR is a set of known reference stars (including their  $x, y, \alpha, \delta$ ) and the  $x, y$  of an object. The object  $x, y$  is found via a fractional aperture centroiding algorithm implemented by the team that operates on a background-subtracted image to accurately determine the center of mass (from an observational perspective) of the object. LSPR calculates “plate constants” for the reference stars, making a model that can translate  $x, y$  coordinates into  $\alpha, \delta$  location. By combining the simultaneous equations into matrices, we find

$$\begin{bmatrix} \sum_i \alpha_i \\ \sum_i \alpha_i x_i \\ \sum_i \alpha_i y_i \end{bmatrix} = \begin{bmatrix} N & \sum_i x_i & \sum_i y_i \\ \sum_i x_i & \sum_i x_i^2 & \sum_i x_i y_i \\ \sum_i y_i & \sum_i x_i y_i & \sum_i y_i^2 \end{bmatrix} \cdot \begin{bmatrix} b_1 \\ a_{11} \\ a_{12} \end{bmatrix} \quad (8)$$

Since all values other than  $b_1, a_{11}$ , and  $a_{12}$  are known, the  $3 \times 3$  matrix can be inverted and  $b_1, a_{11}$ , and  $a_{12}$  can be found. A similar matrix can be created for declination, allowing all six plate constants to be determined. With all six plate constants,

$$\begin{bmatrix} \alpha \\ \delta \end{bmatrix} = \begin{bmatrix} b_1 \\ b_2 \end{bmatrix} + \begin{bmatrix} a_{11} & a_{12} \\ a_{21} & a_{22} \end{bmatrix} \cdot \begin{bmatrix} x \\ y \end{bmatrix} \quad (9)$$

can be used to determine the  $\alpha$  and  $\delta$  of an object. Additionally, the uncertainty of the model can be determined from

$$\sigma_\alpha = \sqrt{\frac{1}{n-3} \sum_i (\alpha_{actual} - \alpha_{fit})^2} \quad (10)$$

with a symmetric equation existing to determine  $\sigma_\delta$ . Finally, one must consider that the image is a two-dimensional projection of a portion of the surface of a sphere. To correct for this, one must flatten the coordinate system, run LSPR, and unflatten the results for what (hopefully) has a more accurate value. The team opted to use LSPR with a flattening correct for all of astrometric data.

### 3.3 Photometry

Again, with processed images, a procedure called Aperture Photometry allows for the visual magnitude of objects in astronomical images to be estimated. By comparing with known values, linear regression can be used to create a fit line for signal (the amount of analog digital counts within an aperture) to visual magnitudes from a photometric catalog. After identifying 2002 QF15 in images, the team found various reference stars and implemented a fractional aperture to allow for optimal precision in photometry. We plotted  $\log_{10}(\text{Signal})$  vs. apparent magnitude for our linear regression. given the zero-point offset correspondence between apparent magnitude and  $-2.5 \log_{10}(\text{Signal})$ , we would expect our linear regression to have a slope of  $-2.5$  and some y intercept for 0 point. For every photometry run, we used five different stars to form our reference set, focusing on creating a large baseline between our brightest and least bright stars. All of our linear regression-based photometry estimations were within 0.25 magnitudes of JPL’s predicted value.

### 3.4 Orbital Elements

From each of the team members' Method of Gauss programs, the following table of orbital elements was generated. Note that eccentricity is a unitless quantity and ranges from 0 to 1.

Orbital Element	W. Beard	J. Hong	G. Xin	Average	JPL
$a$ (AU)	1.054	1.058	1.058	1.056	1.057
$e$	0.343	0.345	0.345	0.344	0.344
$I$ ( $^{\circ}$ )	25.060	25.221	25.221	25.167	25.154
$\Omega$ ( $^{\circ}$ )	236.337	236.258	236.258	236.284	236.257
$\omega$ ( $^{\circ}$ )	255.115	255.533	255.533	255.394	255.516
$M$ ( $^{\circ}$ )	118.811	117.892	117.892	118.193	118.083

Table 2: Observational RA, Dec, and Vmag

### 3.5 Description of Orbital Elements

Classical Keplerian orbits are defined by ellipses: an object (PHA 2002 QF15 for this team) follows an elliptical path with the Sun at one focus. Six parameters are used to uniquely specify this elliptical orbit, in shape, size, orientation with respect to the ecliptic plane, and the position of the asteroid at a given time.

$a$  is the semimajor axis of the elliptical orbit and is used to describe the size of the orbit.  $a$  is typically given in astronomical units (AU). Given position vector  $\vec{r}$  and velocity vector  $\dot{\vec{r}}$  and the magnitude of the position vector  $r$ , we can calculate  $a$  to be

$$a = \left( \frac{2}{r} - \dot{\vec{r}} \cdot \dot{\vec{r}} \right)^{-1} \quad (11)$$

$e$  is the eccentricity, which describes the elongation of the ellipse. A perfectly circular orbit has  $e = 0$ , a parabolic orbit has  $e = 1$ , and an elliptical orbit (the type of orbit we are dealing with) has an eccentricity between 0 and 1. Given  $\vec{r}$  and  $\dot{\vec{r}}$ ,  $e$  can be obtained by computing

$$e = \left[ 1 - \frac{|\vec{r} \times \dot{\vec{r}}|^2}{a^3} \right]^{\frac{1}{2}} \quad (12)$$

$i$  is the inclination, the angle between the plane of asteroid's orbit and the ecliptic plane. To obtain  $i$  from the Gaussian Orbital Determination, we let

$$\vec{h} = \vec{r} \times \dot{\vec{r}} = (x, y, z) \times (\dot{x}, \dot{y}, \dot{z}) \quad (13)$$

and then calculate  $i$  by using

$$\cos i = \frac{h_z}{h} \quad (14)$$

A visualization of the orbital elements can be found below.



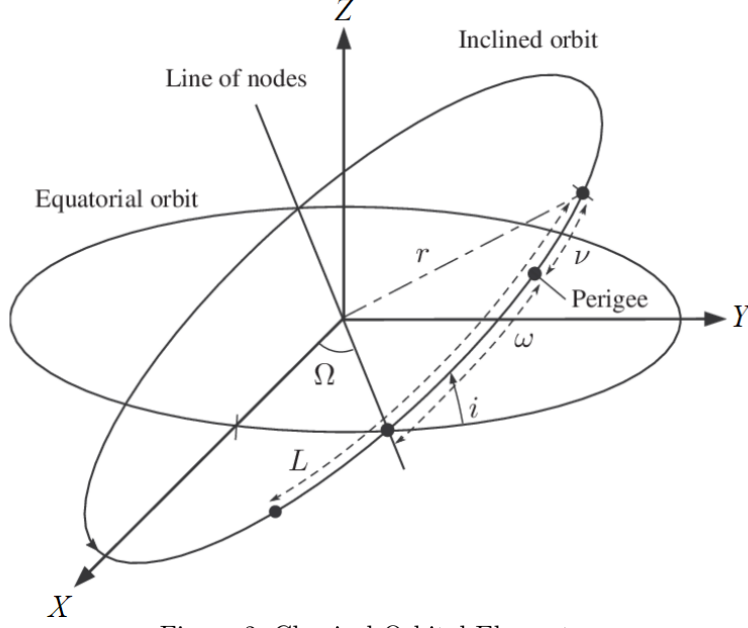


Figure 2: Classical Orbital Elements

$\Omega$  is the longitude of the ascending node, the point at which the orbital and ecliptic planes intersect and the asteroid is moving from “south” to “north” of the ecliptic plane. The longitude is given by the angle between the Vernal Equinox ( $\Upsilon$ ) and the ascending node. To solve for  $\Omega$ , we use the fact that

$$\begin{bmatrix} h_x \\ h_y \\ h_z \end{bmatrix} = R_3 R_2 R_1 \begin{bmatrix} 0 \\ 0 \\ h \end{bmatrix} \quad (15)$$

where  $R_3$ ,  $R_2$ , and  $R_1$  denote rotations about  $\Omega_z$ ,  $i_x$ , and  $\omega_z$  (we will introduce  $\omega$  shortly), respectively. Evaluating the matrix multiplications, we can simplify the above equation to

$$\begin{bmatrix} h_x \\ h_y \\ h_z \end{bmatrix} = \begin{bmatrix} h \sin i \cos \Omega \\ -h \sin i \sin \Omega \\ h \cos i \end{bmatrix} \quad (16)$$

Finally, we use the equations in the matrix above as system of equations to solve for  $\Omega$ .

$\omega$  is the argument of perihelion, the point of closest approach to the sun.  $\omega$  is given by the angle between the asteroid’s ascending node and the perihelion, and is measured eastward in the asteroid’s orbital plane. To calculate  $\omega$ , we introduce a new variable,  $\nu$ , which can be solved for by using

$$\cos \nu = \frac{1}{e} \left[ \frac{a(1-e^2)}{r} - 1 \right] \quad (17)$$

$$\sin \nu = \frac{1}{e} \left( \frac{a(1-e^2)}{h} \right) \left( \frac{\vec{r} \cdot \dot{\vec{r}}}{r} \right) \quad (18)$$

Now let  $U = \nu + \omega$ . We can solve for  $U$  using the following system of equations, and subtract  $\nu$  from  $U$  to obtain  $\omega$ .

$$\cos U = \frac{x \cos \Omega + y \sin \Omega}{r} \quad (19)$$

$$\sin U = \frac{z}{r \sin i} \quad (20)$$

The final orbital element is  $M$ , the mean anomaly. It should be noted that all values for  $M$  in this report display  $M$  precessed to 21 July 2019 06 : 00 UTC. It is the angular position measured from the center of the elliptical orbit eastward from the perihelion point. To calculate  $M$  we first obtain  $E$ , which can be calculated using

$$\cos E = \frac{1}{e} \left( 1 - \frac{r}{a} \right) \quad (21)$$

Then,

$$M = E - e \sin E \quad (22)$$

### 3.6 Comparison With Other Observational Data

Observation	RA <sub>act</sub>	Dec <sub>act</sub>	RA <sub>mod</sub>	Dec <sub>mod</sub>	RA <sub>err</sub> (")	Dec <sub>err</sub> (")
1	14:22:29.87	+23:33:44.4	14:22:29.79	+23:33:42.2	0.08	2.20
2	14:58:40.23	+21:20:16.0	14:58:39.57	+21:20:15.0	0.66	1.00
3	15:07:38.55	+20:27:41.9	15:07:37.58	+20:27:42.3	0.97	0.40

Figure 3: Team #3's Data and Team #9's Model

### 3.7 Differential Correction

Differential corrections are done after the Method of Gauss for orbit improvement. In the Method of Gauss, we have used 3 observations to determine a preliminary orbit; however, we have more data that can be used to improve our predicted orbit.

The Method of Gauss Orbit Determination returns the position vector ( $\vec{r}_2$ ) and the velocity vector ( $\vec{r}_2$ ). Using these vectors and the time of observation in JD, we can find new orbital element values. Then using those new outputs and the Sun Vectors (from JPL Horizons Web Interface), we can use the ephemeris generation to obtain new RA and DEC. Let the new RA be  $\alpha_{\text{fit}}$ , the DEC be  $\delta_{\text{fit}}$ , the RA from the observation be  $\alpha_{\text{obs}}$ , and the DEC from the observation be  $\delta_{\text{obs}}$ . Then, we have

$$\Delta\alpha_i = \alpha_{\text{obs}} - \alpha_{\text{fit}} \quad (23)$$

$$\Delta\delta_i = \delta_{\text{obs}} - \delta_{\text{fit}}. \quad (24)$$

We can also get the partial derivatives using the approximation below:

$$\frac{\partial\alpha_i}{\partial x} \approx \frac{\alpha_i(x + \Delta, y, z, \dot{x}, \dot{y}, \dot{z}) - \alpha_i(x - \Delta, y, z, \dot{x}, \dot{y}, \dot{z})}{2\Delta} \quad (25)$$

where  $\Delta$  is recommended to be about  $10^{-4}$ . We can obtain other partial derivatives using a similar method. Once we have those values, we can compute the following to obtain new  $\Delta x$ ,  $\Delta y$ ,  $\Delta z$ ,  $\Delta \dot{x}$ ,  $\Delta \dot{y}$ , and  $\Delta \dot{z}$ .

$$\begin{bmatrix} \Delta\alpha_i \frac{\partial\alpha_i}{\partial x} \\ \Delta\alpha_i \frac{\partial\alpha_i}{\partial y} \\ \Delta\alpha_i \frac{\partial\alpha_i}{\partial z} \\ \Delta\alpha_i \frac{\partial\alpha_i}{\partial \dot{x}} \\ \Delta\alpha_i \frac{\partial\alpha_i}{\partial \dot{y}} \\ \Delta\alpha_i \frac{\partial\alpha_i}{\partial \dot{z}} \end{bmatrix} = \begin{bmatrix} \left(\frac{\partial\alpha}{\partial x}\right)^2 & \frac{\partial\alpha}{\partial x} \frac{\partial\alpha}{\partial y} & \frac{\partial\alpha}{\partial x} \frac{\partial\alpha}{\partial z} & \frac{\partial\alpha}{\partial x} \frac{\partial\alpha}{\partial \dot{x}} & \frac{\partial\alpha}{\partial x} \frac{\partial\alpha}{\partial \dot{y}} & \frac{\partial\alpha}{\partial x} \frac{\partial\alpha}{\partial \dot{z}} \\ \frac{\partial\alpha}{\partial x} \frac{\partial\alpha}{\partial y} & \left(\frac{\partial\alpha}{\partial y}\right)^2 & \frac{\partial\alpha}{\partial y} \frac{\partial\alpha}{\partial z} & \frac{\partial\alpha}{\partial y} \frac{\partial\alpha}{\partial \dot{x}} & \frac{\partial\alpha}{\partial y} \frac{\partial\alpha}{\partial \dot{y}} & \frac{\partial\alpha}{\partial y} \frac{\partial\alpha}{\partial \dot{z}} \\ \frac{\partial\alpha}{\partial x} \frac{\partial\alpha}{\partial z} & \frac{\partial\alpha}{\partial y} \frac{\partial\alpha}{\partial z} & \left(\frac{\partial\alpha}{\partial z}\right)^2 & \frac{\partial\alpha}{\partial z} \frac{\partial\alpha}{\partial \dot{x}} & \frac{\partial\alpha}{\partial z} \frac{\partial\alpha}{\partial \dot{y}} & \frac{\partial\alpha}{\partial z} \frac{\partial\alpha}{\partial \dot{z}} \\ \frac{\partial\alpha}{\partial x} \frac{\partial\alpha}{\partial \dot{x}} & \frac{\partial\alpha}{\partial y} \frac{\partial\alpha}{\partial \dot{x}} & \frac{\partial\alpha}{\partial z} \frac{\partial\alpha}{\partial \dot{x}} & \left(\frac{\partial\alpha}{\partial \dot{x}}\right)^2 & \frac{\partial\alpha}{\partial \dot{x}} \frac{\partial\alpha}{\partial \dot{y}} & \frac{\partial\alpha}{\partial \dot{x}} \frac{\partial\alpha}{\partial \dot{z}} \\ \frac{\partial\alpha}{\partial x} \frac{\partial\alpha}{\partial \dot{y}} & \frac{\partial\alpha}{\partial y} \frac{\partial\alpha}{\partial \dot{y}} & \frac{\partial\alpha}{\partial z} \frac{\partial\alpha}{\partial \dot{y}} & \frac{\partial\alpha}{\partial \dot{x}} \frac{\partial\alpha}{\partial \dot{y}} & \left(\frac{\partial\alpha}{\partial \dot{y}}\right)^2 & \frac{\partial\alpha}{\partial \dot{y}} \frac{\partial\alpha}{\partial \dot{z}} \\ \frac{\partial\alpha}{\partial x} \frac{\partial\alpha}{\partial \dot{z}} & \frac{\partial\alpha}{\partial y} \frac{\partial\alpha}{\partial \dot{z}} & \frac{\partial\alpha}{\partial z} \frac{\partial\alpha}{\partial \dot{z}} & \frac{\partial\alpha}{\partial \dot{x}} \frac{\partial\alpha}{\partial \dot{z}} & \frac{\partial\alpha}{\partial \dot{y}} \frac{\partial\alpha}{\partial \dot{z}} & \left(\frac{\partial\alpha}{\partial \dot{z}}\right)^2 \end{bmatrix} \cdot \begin{bmatrix} \Delta x \\ \Delta y \\ \Delta z \\ \Delta \dot{x} \\ \Delta \dot{y} \\ \Delta \dot{z} \end{bmatrix} \quad (26)$$

In the matrix above,  $\alpha_i$  is the general symbol for all positional data and hence represents a sum. Let the above matrix be simplified to

$$\mathbf{a} = \mathbf{J}\mathbf{x}. \quad (27)$$

Then to solve for the new position and velocity vectors, which would be given by  $\mathbf{x}$ , we invert  $\mathbf{J}$  as thus:

$$\mathbf{x} = \mathbf{J}^{-1}\mathbf{a} \quad (28)$$

After we get the new  $\vec{r}_2$  and  $\dot{\vec{r}}_2$ , we go back and calculate the new orbital elements.

To determine whether the differential correction has improved the orbit, we need to compare the deviation values before and after the correction. We have already calculated  $\Delta\alpha_i = \alpha_{\text{obs}} - \alpha_{\text{fit}}$  earlier; now we square each and sum them all to get the old

$$\text{RMS}_{\text{orbit}} = \sqrt{\frac{\sum (\alpha_{\text{obs}} - \alpha_{\text{fit}})^2}{n - 6}} \quad (29)$$

where  $n$  is the total number of positional data points. Given  $N$  number of observations, we have an  $(\alpha, \delta)$  pair for each observation; hence,  $n = 2N$ . For us, that means  $n = 2(4) = 8$ .

To get the new  $\text{RMS}_{\text{orbit}}$ , we need to use the ephemeris generation with the newly generated orbital elements to get the new  $\alpha_{\text{fit}}$ . The new RMS should be lower for the differential correction to have been meaningful.

Based on our data, differential correction failed to yield usable adjustments to our Sun-Asteroid vectors as our original vectors were accurate to our additional data point. The correction outputted for  $\dot{\vec{r}}$  seemed reasonable; however, after calculating the RMS of our data before and after correction, we found that our RMS increased (albeit be a factor of  $10^{-15}$ ).

### 3.8 Monte Carlo Error

From LSPR, we have an angular position and an uncertainty in that position. If we center a Gaussian distribution about the angular position with a standard deviation equal to the uncertainty, we can randomly sample the distribution to perform a Monte Carlo error analysis. For all six observational data points entering the Method of Gauss (three right ascensions and three declinations), each can be adjusted by randomly sampling its Gaussian. We arbitrarily chose W. Beard's orbit determination code to run Monte Carlo on. The results of each trial of Monte Carlo (three million total) were saved to files. Histograms were then created for each orbital element, and the standard deviation of the data sets was calculated. For every orbital element, JPL's value was within W. Beard's Full Width at Half Maximum.

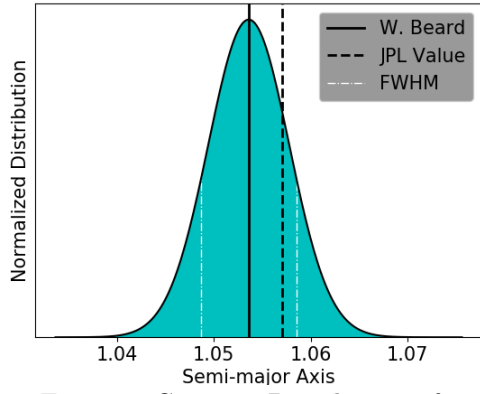


Figure 4: Gaussian Distribution of  $a$

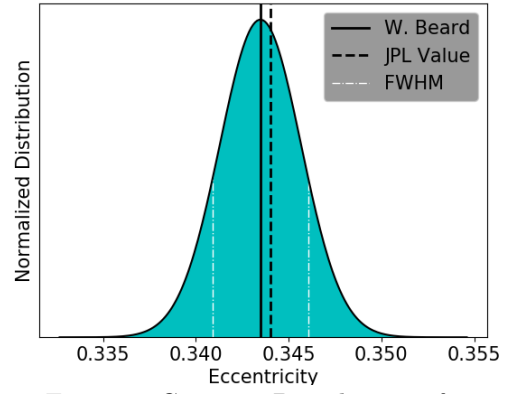


Figure 5: Gaussian Distribution of  $e$

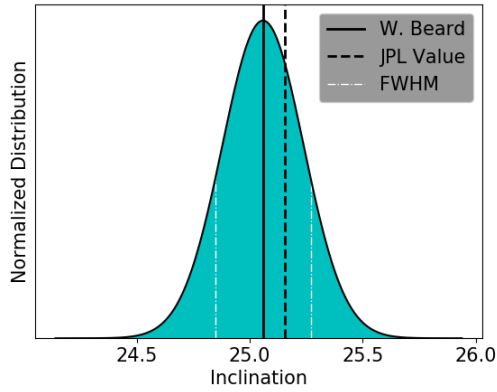


Figure 6: Gaussian Distribution of  $I$

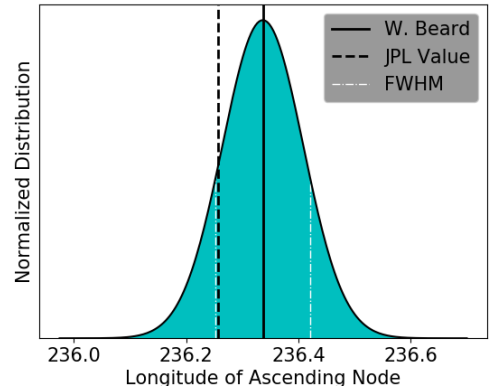
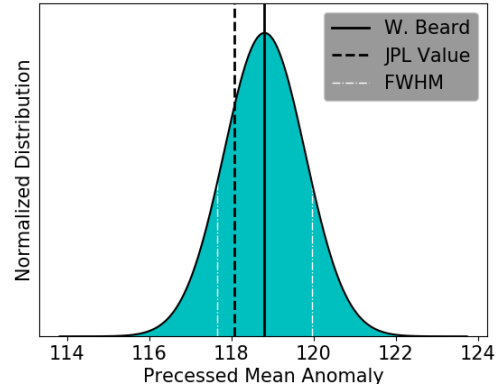
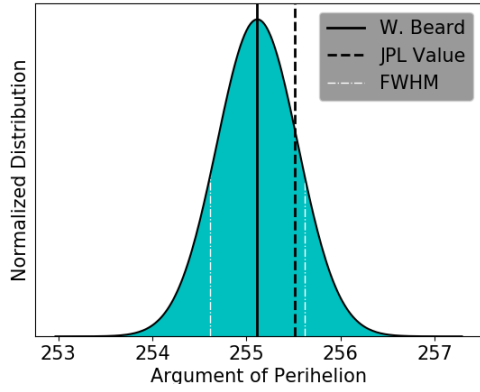


Figure 7: Gaussian Distribution of  $\Omega$



### 3.9 Monte Carlo Adjustment

By using Monte Carlo to generate orbital elements, each set can be tested against multiple data points to obtain an RMS value. With three million Monte Carlo sets, we adjusted W. Beard's data and found a mixed result. The below table shows the adjusted values.

	$a$ (AU)	$e$	$I$ ( $^{\circ}$ )	$\Omega$ ( $^{\circ}$ )	$\omega$ ( $^{\circ}$ )	$M$ ( $^{\circ}$ )
$\sigma$ (W. Beard)	1.059	0.346	24.963	236.227	255.680	117.616

Table 3: W. Beard's Monte Carlo Adjusted Data

While some values improved, others tended away from JPL's orbital elements. After finding this set of Monte Carlo Adjusted orbital elements, one more change that could prove beneficial would be to try  $2^6$  more combinations (every possibility with our starting set and the final set to find an overall best set). While we were not able to further explore this idea, we would like to describe an iterative process that could potentially further improve RMS values. While sampling a Gaussian distribution of the results of the above process would be impossible (there is only one data point: the orbital elements that yielded a minimum RMS), one could sample a uniform distribution of some size centered around the Monte Carlo Adjustment output value. From each of these (one per orbital element), the above process (from sampling on) could be repeated. The person performing this iterative process should use an odd number of points in his/her uniform distribution. This ensures that the original input to the second stage of the iterative process is a possibility for minimum RMS. The process of selecting the minimum RMS orbital elements is repeated until the same set of orbital elements (or similar to some degree of tolerance) is chosen twice in a row. Of course, the more data points that are sampled, the more accurate the final value of this potential process could be.

### 3.10 Other Asteroid Characteristics

Based on our team's average orbital elements and the orbital elements of Earth, orbit visualizations were created. The Sun (center), the Earth (black), and 2002 QF15 (grey) are pictured from two perspectives below.

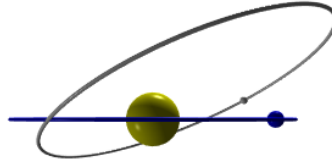


Figure 8: 2002 QF15 From an Ecliptic Perspective

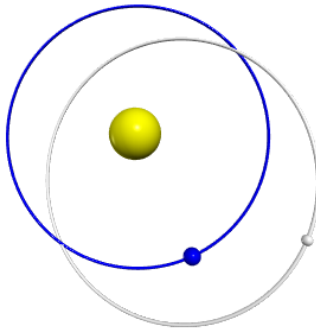


Figure 9: 2002 QF15 From a Bird's Eye Perspective

Finally, we found the period of 2002 QF15 to be 1.081 years by converting the mean motion into years per orbit.

### 3.11 Comparison With Known Values

To begin, we considered the uncertainty present in our own data. From the data created by Monte Carlo, simple statistical analysis allows standard deviation to be calculated for each orbital element. These values are displayed in the table below.

	$a$ (AU)	$e$	$I$ ( $^{\circ}$ )	$\Omega$ ( $^{\circ}$ )	$\omega$ ( $^{\circ}$ )	$M$ ( $^{\circ}$ )
$\sigma$ (W. Beard)	0.004	0.002	0.180	0.072	0.431	0.988

Table 4: Uncertainty in Orbital Elements (W. Beard’s data)

The uncertainty for each element is low (considering that more volatile elements like  $M$  change rapidly with time), meaning that variation from known values should be minimal. Looking back at Table 2, if we calculate the percent error for each orbital element, we find the following.

	$a$ (AU)	$e$	$I$ ( $^{\circ}$ )	$\Omega$ ( $^{\circ}$ )	$\omega$ ( $^{\circ}$ )	$M$ ( $^{\circ}$ )	Average
% error (Team #9)	0.095	0.000	0.052	0.011	0.048	0.093	0.050

Table 5: Percent Error in Average Orbital Elements with JPL

### 3.12 Near-Earth Asteroid Group

2002 QF15 is an Apollo asteroid. Based on both our data and that of JPL, 2002 QF15 falls into the Apollo designation as its semi-major axis is greater than 1 AU and its perihelion distance is less than Earth’s aphelion distance (1.017 AU). In addition, 2002 QF15 has the designation of being a potentially hazardous asteroid (PHA) as it’s minimum orbit intersection distance (MOID) is 0.0068 AU (PHAs must have an MOID less than 0.05 AU) and it has an absolute magnitude less than 22.

## 4 Conclusion

Our orbital element values are both precise and accurate, considering the low errors (all orbital elements are within 0.1% error) when compared with known values.

While we had a total of five usable data sets from our clear-night observations, we do believe more usable data would have been helpful in increasing our orbital elements’ accuracy. Even so, we recognize that there will still be some unavoidable error in part due to the limitations in our observation equipment and imperfections in computations.

For future replications of this research, we recommend following all directions and procedures carefully and taking great care when programming the necessary methods such as the LSPR, Gaussian Orbit Determination, astrometry, and aperture photometry. As much of the code written at SSP is self-reliant (i.e. an ephemeris generator might be used later on in a Monte Carlo Adjustment), extreme caution is paramount to continued success throughout longer periods of research.

## 5 Appendices

### 5.1 Minor Planet Center Report

The following report was submitted to the Minor Planet Center on 7/18/2019.

COD 719  
CON A. W. Rengstorf  
CON [adamwr@pnw.edu]  
OBS W. Beard, J. Hong, G. Xin  
MEA W. Beard, J. Hong, G. Xin  
TEL 0.36-m f/11 reflector + CCD  
NET GAIA DR2  
NUM 6  
ACK Team #9 - 2002 QF15

68950	2019 06 21.16355	14 28 02.03	23 21 44.8	16.2 V	719 2019 06 21 03:55:31
68950	2019 06 21.20528	14 28 08.23	23 21 27.8	16.4 V	719 2019 06 21 04:55:36
68950	2019 06 30.15979	14 48 45.81	22 10 04.4	17.1 V	719 2019 06 30 03:50:06
68950	2019 06 30.20294	14 48 50.85	22 09 39.9	16.9 V	719 2019 06 30 04:52:14
68950	2019 07 04.24910	14 56 44.59	21 30 43.3	17.1 R	719 2019 07 04 05:58:42
68950	2019 07 04.27694	14 56 47.62	21 30 25.8	17.2 R	719 2019 07 04 06:38:48

Figure 10: MPC Report - Team #9

## 5.2 Cloudy Night Experiments

### 5.2.1 Data Collection Strategy

We had three clouded out observation sessions from June 20, 2019 to July 11, 2019. We used the Celestron C-14 telescope at Etscorn Observatory to take dark images and biases for our cloudy night analysis. The dates, purposes, conditions, and images of each observation are listed below:

#	Time (UTC)	Relationship	Conditions	Images Taken
1	7/04/19	Dark Current vs.	CCD T = ambient	5 darks per (5, 10,
	5:00-7:00	Exposure Time	T - 5C	20, 40)s, 5 biases
2	7/08/19	Dark Current	time = 120s	5 darks and biases per
	3:00-5:00	vs. Temp		(19, 14, 9, 4, -1, -6)*C
3	7/12/19	Bias Frames	N/A	11 biases per (24, 22, 20, 18,
	3:00-5:00	vs. Temp		16, 14, 12, 10, 8, 6, 4, 2, 0, -2, -4, -6, -8, -10, -12, -14)*C

Table 6: Details of each cloudy night observation

### 5.2.2 Methodology

For each cloudy night, we coded the following procedure in Python to analyze our data:

1. Trim the edges of the images by 20 pixels to avoid edge effects.
2. Find the bias-subtracted signal for the dark images and the signal for the bias images by calculating their average pixel counts.
3. Calculate the uncertainty (i.e the noise) of the signals between each dark or bias image.
  - (a) Create N-1 noise images, where N is the number of dark/bias images.

(b) The uncertainty between two noise images is:

$$\sigma = \frac{|x_2 - x_1|}{\sqrt{2}} \quad (30)$$

We further processed our data to produce unique best-fit graphs for each cloudy night observation, based on the relationship that the observation was intended to investigate. We used functions from the scipy library to graph best-fit lines and quadratic functions for our data.

### 5.2.3 Hypotheses and Expected Results

Before conducting our observations for each cloudy night, we developed hypotheses on the results of our analyses:

1. The longer the exposure time, the more dark current there will be.
2. Dark current will increase linearly along with the temperature of the CCD chip.
3. The temperature of the CCD chip has no effect on the bias frames.

### 5.2.4 Cloudy Night One: Dependence of Dark Currents on Exposure Time.

We set the temperature of our CCD chip to 3°C below the ambient temperature of 22°C (19°C), although the temperature did fluctuate ( $\sim 0.3^\circ\text{C}$ ) throughout our observation. Starting with an exposure time of 5 seconds, we took 5 dark images per series and continued to double the exposure time for the each next series. We also made sure to take a set of biases to calculate the noise of the images. Our final full set of darks had an exposure time of 40 seconds. We were only able to take four full sets of dark images, however, as the sky cleared up and we moved on to taking sets of our asteroid.

Figure 11 plots the dark current (the average pixel count) of each image against the exposure time at which it was taken:

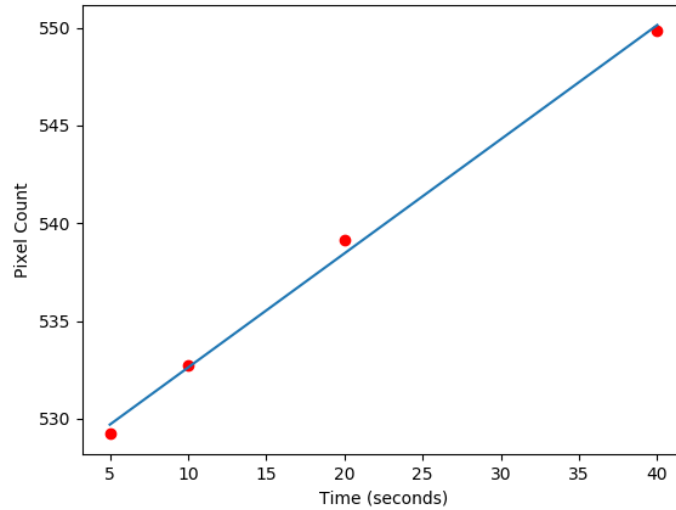


Figure 11: Cloudy Night 1 - Dark Current vs Time with Constant Temperature

Best Fit Line:  $y = mx + b$

Slope (m): 0.584031

Intercept (b): 526.780

Coefficient of Determination ( $r^2$ ): 0.996725



The linear regression function from the SciPy library produced a best-fit line that very closely represents the data points we plotted, and the line confirms our hypothesis that the dark current has a positive linear relationship with exposure time.

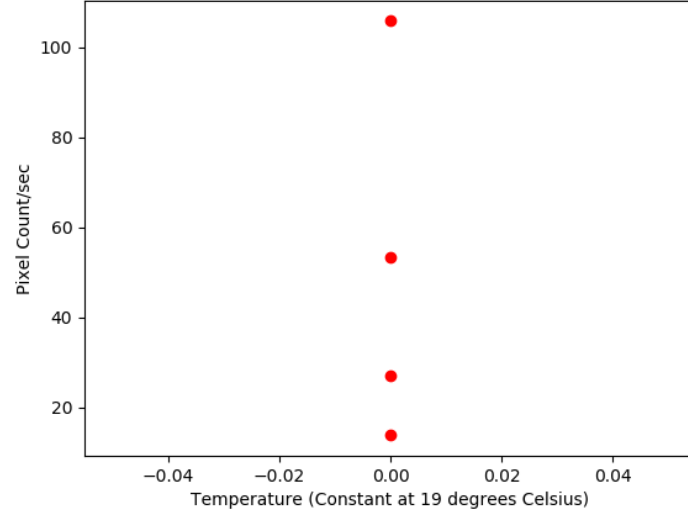


Figure 12: Cloudy Night 1 - Pixel Count/second vs. Constant Temperature

Figure 12 plots the pixel count divided by the exposure time for each image against the constant CCD chip temperature. The result is a vertical line of data points that have an exponentially increasing amount of pixel counts per second.

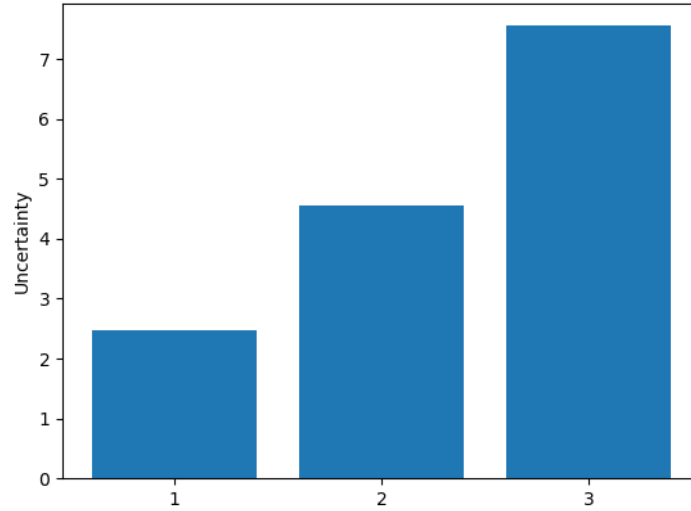


Figure 13: Cloudy Night 1 - Uncertainty Trend

Finally, we plotted a bar chart of our signal uncertainties (noises) between each image, which is shown in Figure 13. We concluded that the uncertainty of the images increases somewhat exponentially.

### 5.2.5 Cloudy Night Two: Temperature Dependence of Dark Frames

We held the exposure time of the darks at a constant 120 seconds throughout this observation as we were varying the temperature of the CCD chip. Our starting temperature was 19°C, which was 3°C below the ambient temperature. We continued decreasing the temperature of the chip by 5°C after taking 5 bias and dark images. The temperature of the chip varied by  $\sim 0.5^\circ\text{C}$  for each series. Although ideally we would have liked to continue decreasing the temperature until the chip's cooling capacity was exceeded, we ran out of time and ended with a temperature of  $-11^\circ\text{C}$ , at a cooling power

of  $\sim 61.5\%$ . Figure 14 plots the the dark current against the temperature of the CCD chip when it was taken:

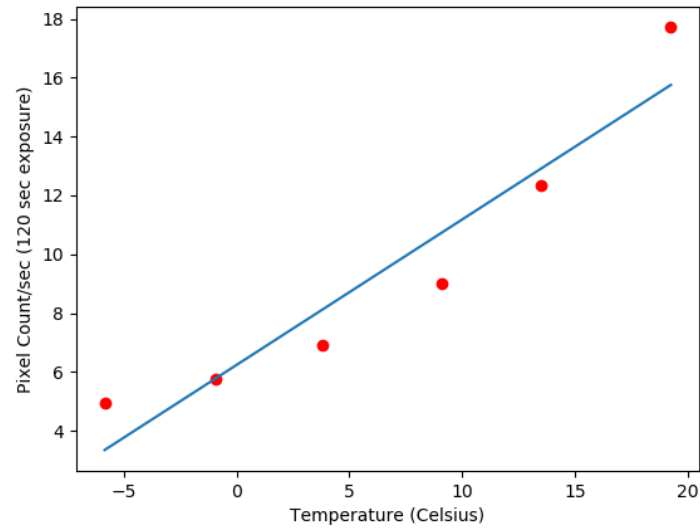


Figure 14: Cloudy Night 2 - Dark Current vs. Temperature

Best Fit Line:  $y = mx + b$

Slope (m): 0.494134

Intercept (b): 6.24327

Coefficient of Determination ( $r^2$ ): 0.904198

Through simple visual inspection, it is evident that a linear relationship is not the best fit for this data - a quadratic equation would serve as a better fit for the graph.

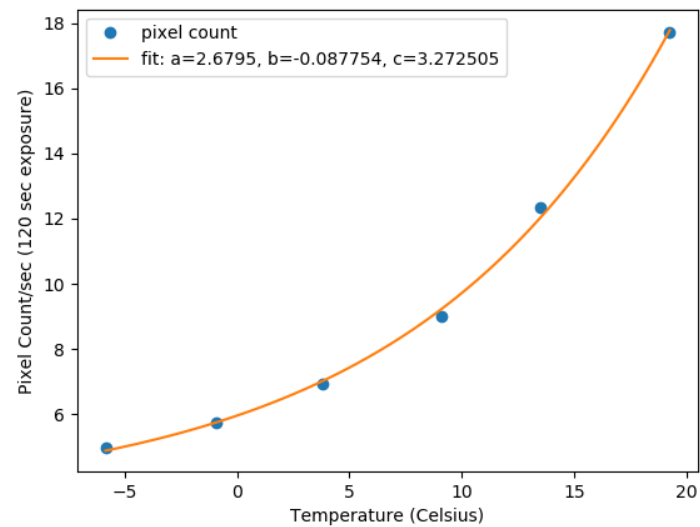


Figure 15: Cloudy Night 2 - Dark Current vs Temperature (Quadratic Fit)

We used the SciPy module `curve_fit` to create Figure 15, which fits a quadratic function rather than a linear best-fit line to our data.

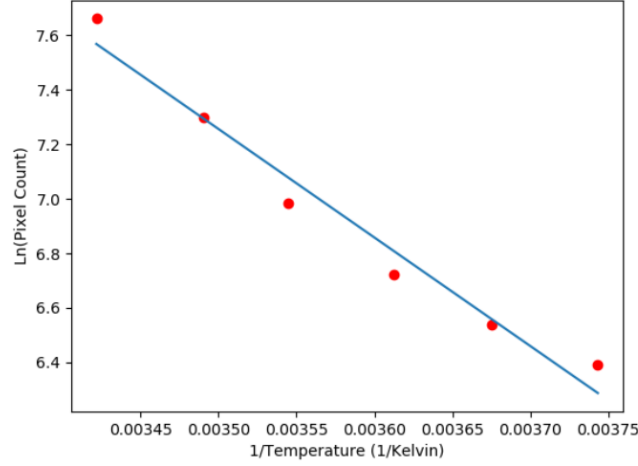


Figure 16: Cloudy Night 2 - Natural log of Dark Current vs. Inverse of Temperature

Best Fit Line:  $y = mx + b$

Slope (m): -3986.30

Intercept (b): 21.2088

Coefficient of Determination ( $r^2$ ): 0.969659

The figure above shows an inverse linear relationship between  $\ln(\text{Pixel Count})$  and  $1/T$ , which agrees with the Arrhenius law. With the information from this graph, we calculated the activation energy  $\Delta E$  of the CCD chip with the following derivation:

$$De^- = De_o^- \cdot e^{\frac{-\Delta E}{kT}} \quad (31)$$

$$\ln(De^-) = \ln(De_o^-) + \frac{-\Delta E}{kT} \quad (32)$$

$$y = \ln(De^-) \quad (33)$$

$$b = \ln(De_o^-) \quad (34)$$

$$m = \frac{-\Delta E}{k} \quad (35)$$

$$x = \frac{1}{T} \quad (36)$$

$$\Delta E = -m \times k \quad (37)$$

where  $k$  is the Boltzmann constant ( $1.38065 \cdot 10^{-23} \frac{m^2 kg}{s^2 K}$ ). Our activation energy was calculated to be  $5.50109 \cdot 10^{-20} \text{ V}$ , or  $0.343389 \text{ eV}$ .

We can also graph the relationship between  $\ln(De_o^-)$  against  $\Delta E$ . From the equation

$$De_o^- = De_{00}^- e^{\frac{\Delta E}{E_{MN}}} \quad (38)$$

we can derive

$$\ln\left(\frac{De_o^-}{De_{00}^-}\right) = \frac{\Delta E}{E_{MN}} \quad (39)$$

$$\ln(De_0^-) = \ln(De_{00}^-) + \frac{\Delta E}{E_{MN}} \quad (40)$$

Hence when each individual datapoint is plotted, we get a linear shape as shown below.

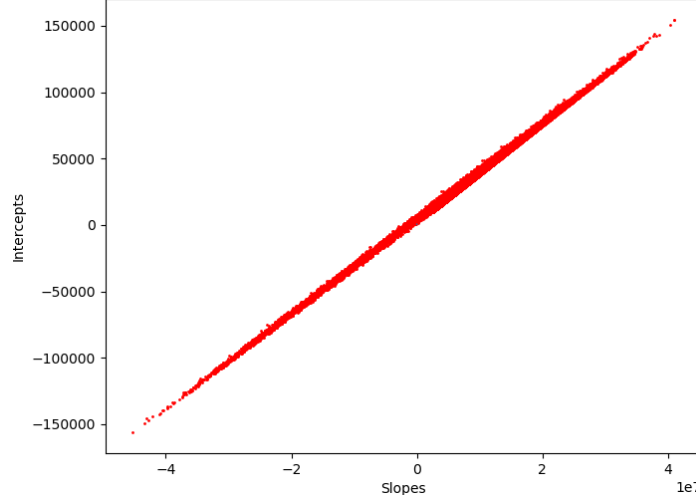


Figure 17: Cloudy Night 2 -  $\ln$  of Exponential Prefactor  $De_0^-$  vs Activation Energy

Furthermore, from (34) we determined that the y-intercept of Figure 16,  $b$ , is equal to the natural log of the exponential prefactor. From there, we calculated the exponential prefactor as  $1.62503 \cdot 10^{10}$  from the following equation:

$$De_o^- = e^b \quad (41)$$

After calculating the activation energy and exponential prefactor for the CCD chip as a whole, we move on to calculate the isokinetic temperature,  $T_{MN}$ . This is the temperature at which the dark current is independent of the activation energy. We know that

$$T_{MN} = \frac{E_{MN}}{k} \quad (42)$$

and we also know that

$$De_0^- = De_{00}^- e^{\frac{\Delta E}{E_{MN}}} \quad (43)$$

where  $De_{00}^-$  is the dark current at the isokinetic temperature. Taking the  $\ln$  and rearranging, we get

$$\ln(De_0^-) = \ln(De_{00}^-) + \frac{\Delta E}{E_{MN}} \quad (44)$$

Graphing  $\ln(De_0^-)$  against  $\Delta E$  (the values we have from previous equation), we get a linear line with slope  $m_2$  equal to  $\frac{1}{E_{MN}}$ . Then

$$T_{MN} = \frac{1}{\frac{m_2}{k}} \quad (45)$$

Computing our  $T_{MN}$  in the manner above, we found our final isokinetic temperature to be 269.468 K, or -3.532°C.

Now we determine our uncertainties. We again plotted a bar chart of our signal uncertainties:

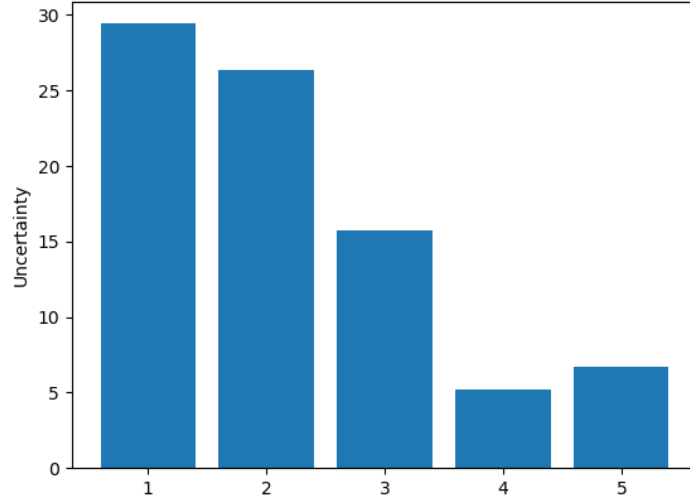


Figure 18: Cloudy Night 2 - Uncertainty Trend

Aside from the last uncertainty, all the data points seem to show that the uncertainty is decreasing at an exponential rate.

### 5.2.6 Cloudy Night Three: Constancy of the Bias Levels

Since bias frame's exposure time is constant 0.0 seconds, we varied the chip temperature to find their dependence. Starting at 3C° below the ambient temperature, at 24C°, we took a series of 11 bias images. Then we reduced the temperature by 2C and allowed the temperature to stabilise before taking another set of 11 bias images and repeated the process. Again, ideally the process was to be repeated until the chip's cooling capacity was exceeded, but we aborted the cloudy night session after taking the 20<sup>th</sup> bias set at temperature -14C° and power 81% to take series of our asteroid.

As our hypothesis for this cloudy night experiment was that bias frames do not depend on temperature, we expected that the slope of our bias pixel count vs. temperature graph (Figure 19) below to be closer to zero than the uncertainty on the slope.

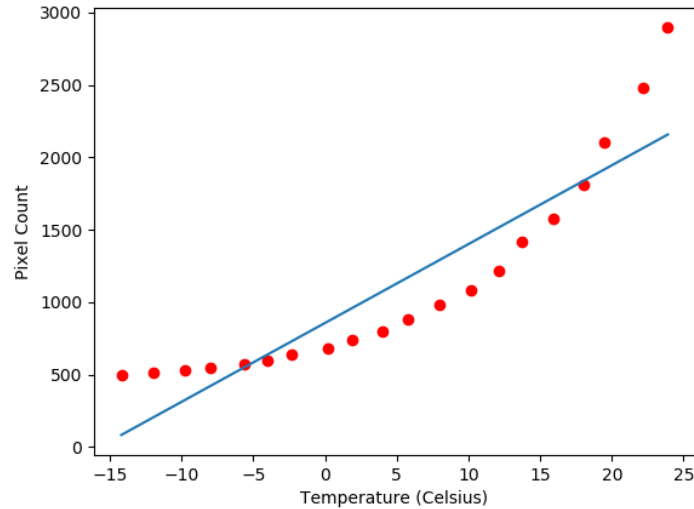


Figure 19: Cloudy Night 3 - Biases vs. Temperature

Best Fit Line:  $y = mx + b$

Slope (m): 83.02494108018769

Intercept (b): 1306.4570977047908

Coefficient of Determination ( $r^2$ ): 0.8231473523966603

Although a linear line is not the best fit for this data, the non-zero slope and the evident curve in the graph mean that the bias frames are, in fact, not independent from the temperature of the CCD chip. We used a quadratic curve to give our data a better fit:

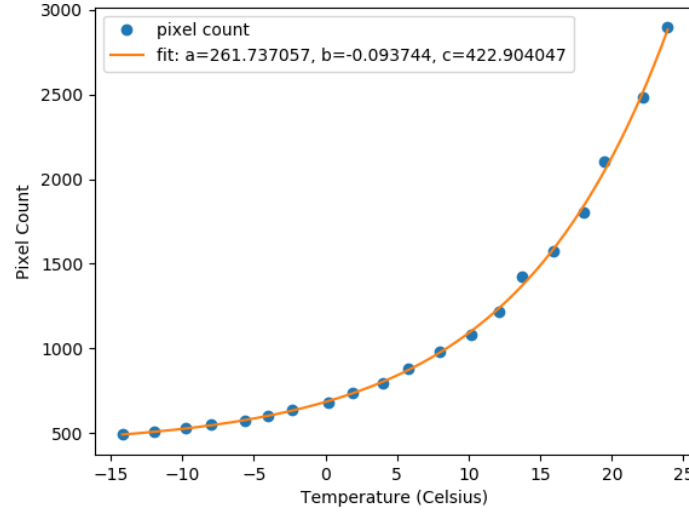


Figure 20: Cloudy Night 3 - Biases vs. Temperature (Quadratic Fit)

This curve fits almost perfectly, confirming that there is a definite relationship between the bias frames and the temperature of the chip, and therefore proving our hypothesis wrong. Lastly, we graphed our bar chart of signal uncertainties:

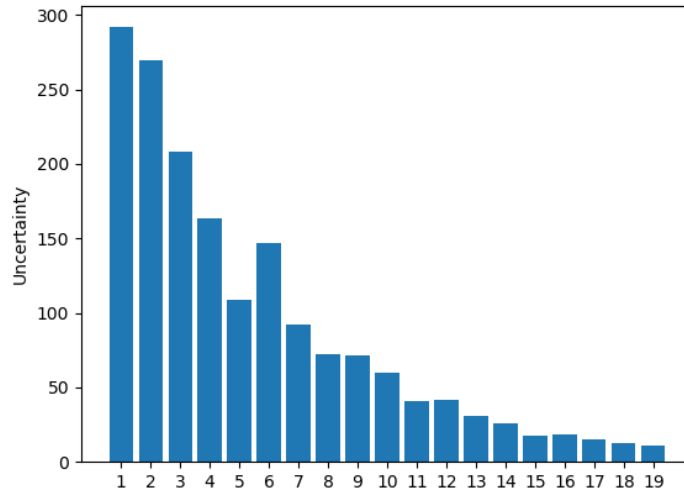


Figure 21: Cloudy Night 3 - Uncertainty Trend

We concluded that the uncertainty decreases at a decreasing rate.

## 6 Acknowledgements

We would very much like to thank the faculty and staff of New Mexico Tech and the Summer Science Program '19 who gave us the opportunity to learn about, find, and track an asteroid during our summer. Specifically, Dr. Andersen, Mrs. Martinez, and Dr. Rengstorf were always dedicated to making sure SSP was not only a powerful period of academic growth for its participants but also a resounding time of *personal* growth. With a warm heart for all of the TAs (Cyndia Cao, Anthony Flores, Descartes Holland, and Emma Loudon), we would like to conclude our Orbit Determination

report with the lasting thought of the impact SSP has made on us, that which it made participants of the past, and that which it *will* make on participants of the future. From Team #9 - Thank you.

## References

- [2019] A. Rengstorf et al., “Orbit Determination Packet”, Summer Science Program Astrophysics
- [2004] M. Paine, “Environmental Damage from Asteroid and Comet Impacts”, UC Museum of Paleontology
- [2017] M. Leomanni, Classical Orbital Elements, “A Class of Globally Stabilizing Feedback Controllers for the Orbital Rendezvous Problem”, Universit’a di Siena
- [2019] JPL, “JPL Small-Body Database Browser - 68950 (2002 QF15)”
- [2002] R. Widenhorn, “Temperature dependence of dark current in a CCD”